JGR Solid Earth

RESEARCH ARTICLE
10.1029/2018JB016959

Short Timescale Analysis of Microseisms and Application to Array Calibration

M. Gal[1,2], A. M. Reading[1], and S. P. Ellingsen[1]

[1]School of Natural Sciences (Physics), University of Tasmania, Hobart, Tasmania, Australia, [2]Institute of Mine Seismology, Kingston, Tasmania, Australia

Key Points:
- First seismic array observations of microseisms on short timescales
- Microseisms are found to propagate as pulses of coherent energy
- Pulses can be used to calibrate seismic array

Supporting Information:
- Supporting Information S1

Correspondence to:
M. Gal,
martin.gal@utas.edu.au

Citation:
Gal, M., Reading, A. M., & Ellingsen, S. P. (2019). Short timescale analysis of microseisms and application to array calibration. *Journal of Geophysical Research: Solid Earth*, *124*, 2684–2701. https://doi.org/10.1029/2018JB016959

Received 31 OCT 2018
Accepted 13 FEB 2019
Accepted article online 14 FEB 2019
Published online 6 MAR 2019

Abstract Primary and secondary microseisms are analyzed in this study using a novel matched field processing approach that allows for analysis of features with temporal scales of the order of seconds. The majority of previous microseism research employs time averaging; hence, very little is currently known about the properties of the wavefield on such short timescales. We aim to better understand the nature of the microseismic wavefield through applying our novel matched field processing approach to example data from two seismic arrays (USArray and Rio Grande Rift-Flex Array) in the United States. We find that surface and body wave microseisms on short timescales are observed as pulses of coherent energy, which may be separated in time, embedded in the continuous signal. The pulses display a much larger coherence value in comparison to the commonly employed time averaging approaches, given that they can be separated in time. This allows us to study the spatial correlation of the wavefield and gives an insight into the source and path propagation effects of surface and body waves. We find that the correlation of the short timescale surface wavefield between two stations is dependent on the distance between them and is strongly dependent on their geometric position with respect to the source. Correlations on the *PKP* wavefield show a decrease with increasing source-station distance and a mild decrease for azimuthally distributed stations at the same source-station distance. Finally, we demonstrate how the pulse wavefield can be used for array calibration purposes.

1. Introduction

Over recent decades, the study of microseisms has increased in popularity and becomes a major contributor to the field of seismology. Historically regarded as noise, microseisms are continuous seismic oscillations in the form of surface and body waves with an origin in the oceans (Gutenberg, 1936; Hasselmann, 1963; Haubrich et al., 1963; Lacoss et al., 1969; Longuet-Higgins, 1950; Toksöz & Lacoss, 1968; Wiechert, 1904) and lakes (e.g., Koper et al., 2009). The microseisms signal is dominant in the period range of 0.5–20 s (McNamara & Buland, 2004) without the presence of earthquakes and can be classified by two distinct spectral features (Berger et al., 2004) which can be attributed to differing excitation mechanisms (Ardhuin et al., 2015). Primary microseisms (~10–20 s) are generated by the interaction of the gravity wave stored in the water column and a shallow and wavy bathymetry (Ardhuin, 2018; Ardhuin et al., 2015; Hasselmann, 1963; Haubrich et al., 1963; Saito, 2010) and are the weaker signals in the microseism range. Their period is directly proportional to the ocean gravity waves that excite them. Secondary microseisms (~0.5–10 s) are generated by the interaction of two interfering swell trains when the resulting wavenumber approaches velocities comparable to the one of seismic waves (Ardhuin et al., 2015; Longuet-Higgins, 1950). Their period range is half that of the ocean swell. Additionally, resonance effects in the water column play an important role for an effective transfer to the solid Earth (Gualtieri et al., 2013; Longuet-Higgins, 1950).

Microseism sources have been extensively investigated with single station (e.g., Bromirski & Duennebier, 2002; Koper & Burlacu, 2015; Schimmel et al., 2011; Schulte-Pelkum et al., 2004; Stutzmann et al., 2012, 2000, 2009) and array methods (e.g., Euler et al., 2014; Farra et al., 2016; Friedrich et al., 1998; Gal et al., 2015, 2018; Gerstoft et al., 2008; Koper et al., 2010; Landès et al., 2010; Liu et al., 2016; Reading et al., 2014) to estimate their spatial generation location and temporal variability and compare their observed power to hindcast models (Farra et al., 2016). One of the most significant findings in the last two decades in the field of microseisms was that one can estimate the approximate interstation Green's function between two receivers by cross correlation of their respective microseism wavefields (Campillo & Paul, 2003; Shapiro & Campillo,

©2019. American Geophysical Union. All Rights Reserved.

2004; Snieder & Hagerty, 2004; Roux et al., 2005) which makes it possible to extract information on the medium between the stations. This finding led to transformational research in seismic tomography (e.g., Shapiro & Campillo, 2004), cross-correlation sensitivity kernels (e.g., Tromp et al., 2010), volcano monitoring (e.g., Snieder & Hagerty, 2004), and exploration applications (e.g., Legaz et al., 2009; Vandemeulebrouck et al., 2010).

A common denominator in the majority of the above studies is temporal averaging which provides robust results in the case of beamforming and cross-correlation techniques. While this allows the capture of persisting patterns in the wavefield, very little is known about the wavefield on short timescales. To our knowledge only one single station polarization technique (Schimmel et al., 2011) has been employed to analyze the microseism wavefield on the order of seconds. It makes use of high time resolution to identify segments in the wavefield which follow the mechanics of Rayleigh waves (degree of polarization) for a more robust back azimuth estimation.

In this work, we will analyze the microseism wavefield on short timescales (order of seconds) with seismic array techniques (Rost & Thomas, 2002, 2009; Gal & Reading, 2018). We have designed a novel framework which makes use of three main components: (1) The analytical signal representation obtained via the Hilbert transform to estimate the time-frequency representation of the wavefield, (2) fast marching (Rawlinson & Sambridge, 2005) in combination with a phase velocity map used to generate source traveltimes, and (3) used as input into a matched field processing (MFP) beamformer (Gal et al., 2018). The novel approach is first tested on an earthquake example and is then applied to the analysis of the primary and secondary microseism wavefields to infer its properties on short timescales. Finally, we demonstrate how the short timescale wavefield can be used to calibrate a seismic array.

2. Method

To study the microseism wavefield on short timescales with seismic array beamforming, a modification of the conventional approach is required. First, we lay out single component beamforming and the required modifications to adapt it to short-time signals followed by the extension to three components.

2.1. Conventional Beamforming

The beam power of the single component frequency wavenumber analysis (also known as Bartlett beamfoming / processor) is defined as

$$P(\vec{s}, f) = \frac{1}{K} \sum_n \sum_m C_{nm}(f) e^{-2\pi i f \vec{s}(\vec{r}_m - \vec{r}_n)}, \tag{1}$$

where $C_{nm}(f)$ denotes the cross-power spectral density matrix, $\vec{s}$ is the slowness vector, f is the frequency, $\vec{r}$ is the position of the seismic station, and K is the number of stations. An alternative but more intuitive notation of the beam power can be expressed via the direct use of the Fourier transformed data vector $X(f)$

$$P(\vec{s}, f) = \frac{1}{K^2 L^2} \left| \sum_n e^{-2\pi i f \vec{s} \vec{r}_n} X_n(f) \right|^2, \tag{2}$$

where L is the number of data points (snapshot length/temporal window length) of the observed signal $x(t)$. This representation shows that the underlying principle of beamforming is a simple correlation between a plane wave and the spectral representation of the observed seismic data. The beam power is maximized if the complex product between the two entities results in the same complex phase per summation step n, which is the case if the predicted phase delay matches the one from the observed spectral wavefield $X_n(f)$ at each seismic station. It is furthermore possible to transform the product between the position $\vec{r}$ and slowness $\vec{s}$ into the traveltime t, given the same dimension (second). These two approaches are identical for a farfield source and homogeneous velocity, but for sources in the nearfield or inhomogeneous velocities, which result in a nonplanar wave propagation over the array, the use of the traveltime (under the assumption of a known phase velocity) is advantageous. This modification generalizes beamforming into the class of MFP (e.g., Baggeroer et al., 1993) and has been previously used for exploration purposes (e.g., Corciulo et al., 2012) and the analysis of microseisms (e.g., Gal et al., 2018). Hence, the underlying base equation which we will adapt in the following for the analysis of short-time microseisms is defined as

$$P(\vec{s}, f) = \frac{1}{K^2 L^2} \left| \sum_n e^{-2\pi i f t_n(x,f)} X_n(f) \right|^2, \tag{3}$$

where x is the spatial location where the beam is focused and $t_n(x,f)$ is the corresponding traveltime for a given phase velocity model.

2.2. Short Timescale Modifications

To evaluate seismic array data on short timescales, it is required to modify the conventional data preparation steps. Usually when beamforming is applied to microseisms, the seismic data $x(t)$ are cut into snapshots with a duration that ranges from minutes to hours. A longer snapshot length results in a more detailed spectral representation but suffers from low temporal resolution and vice versa. As we are interested in a high time resolution, we are required to choose the snapshot length as short as possible which can be accomplished with methods such as the short-time Fourier transform, S-transform, wavelet transform, or the analytical signal representation.

Given that beamforming and MFP are narrowband techniques, snapshots which have a duration equal to the period of interest have a very crude frequency representation, resulting in a large mix of frequencies in a single frequency bin, which likely degrades the performance of the narrowband beamforming, and hence, it is necessary to prefilter the raw seismic data in order to obtain a narrowband representation before the generation of snapshots. Care must be taken with this approach, as prefiltering to a narrow frequency range again delocalizes the signals content in time.

We have applied the short-time Fourier transform, S-Transform, and the analytical signal representation in combination with prefiltering and found that the three methods yield very similar results for the intended task. Overall, we find the analytical signal representation to be most suitable with respect to computation time and memory requirements and select it for our MFP framework.

The second modification is the temporal alignment of seismic traces for a given spatial location. Since we are interested in short timescales, signals that propagate from location x toward each sensor require a different traveltime. Let us assume that there are two sensors separated by a distance d with respect to the source direction. A pulse of energy reaches the first sensor at time t_1 and the second sensor at $t_2 = t_1 + |\vec{s}|d$. If we were to apply conventional MFP, the pulse might not have time to reach both sensors within the time of the snapshot length, which would lead to two differing wavefields being analyzed. Instead of computing MFP for each sensor at the same time, we define a source time t_s and align all seismic traces given their traveltime to the source point x with $T(x) = t_s + t_n(x)$.

The above procedure can be summarized as follows:

1. The raw seismic data $x(t)$ are prefiltered in the frequency range of interest to form $\tilde{x}(t)$.
2. $\tilde{x}(t)$ is used as input to generate the analytical signal via the Hilbert transform $\tilde{X}(f,t)$.
3. The MFP beam power is obtained from $P(f, T(x)) = \frac{1}{K^2} \left| \sum_n \tilde{X}(f, T(x)) \right|^2$.

Note that the plane wave term (or MFP replica vector) is not present as we have aligned all traces according to a propagation model; hence, the exponential function is reduced to a simple value of 1. The extension to three components then is

$$P_{3C}(f, T(x)) = \frac{1}{K^2} \left| \sum_n \left[p_Z \tilde{X}_{Zn}(f, T(x)) + p_H (\cos(\theta_n) \tilde{X}_{Nn}(f, T(x)) + \sin(\theta_n) \tilde{X}_{En}(f, T(x))) \right] \right|^2, \tag{4}$$

where p are the polarization coefficients for each component Z, N, and E and θ_n is the back azimuth from the nth station toward the source x for Rayleigh waves and for Love waves an additional 90° angle is added to the back azimuth (i.e., radial and transverse angles). For Rayleigh waves, we can exploit the retrograde motion and set $p_Z = 1$ and $p_H = i$, while for Love waves only the horizontal components are used $p_Z = 0$ and $p_H = 1$. In addition to this main equation, we will make use of two variations to display our results: The coherence, which is obtained by normalizing each sensor component by the combined power of all three components at each time t

$$M(f,t) = \sqrt{\left|\tilde{X}_{Zn}(f,t)\right|^2 + \left|\tilde{X}_{Nn}(f,t)\right|^2 + \left|\tilde{X}_{En}(f,t)\right|^2} \tag{5}$$

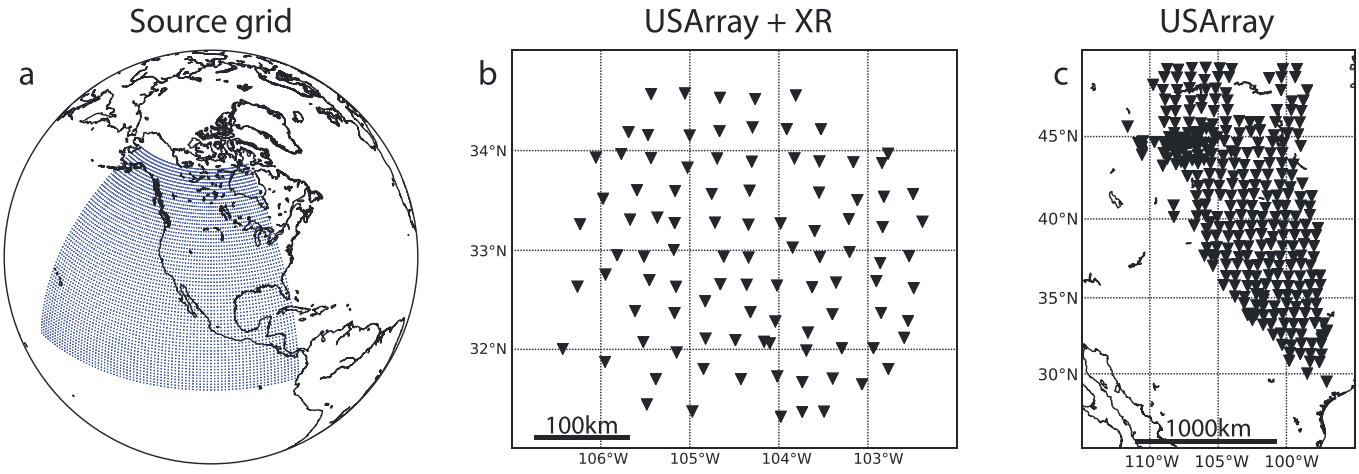

Figure 1. The MFP source grid (a) for the surface waves analysis consists of 66 by 81 points ranging from 5°S to 60°N latitude and 160°W to 80°W longitude (1° grid spacing). We use a combination of USArray and XR stations (b) for the surface wave analysis and a large portion of the USArray (c) for the *PKP* analysis.

and inserting the normalized analytical signal representation into MFP and the total power which is obtained by placing the summation $\sum_n$ in equation (4) outside of the absolute value. This will result in a summation of power independent of the phase and will be useful in later discussion. It should be noted that the coherence here differs from the usual use in beamforming where a time window is Fourier transformed and normalized. Here the normalization is taken for every time t (i.e., every data point).

2.3. Example Data

We select North America as our study area since it has been extensively studied (multiple seismic tomography data sets are freely available), and the USArray was deployed over a large area which gives us the opportunity to study the wavefield over a large spatial area. Additionally, we will make use of the XR network (Rio Grande Rift-Flex Array) in combination with the USArray to form a seismic array with an increased number of stations.

For the traveltimes $t_n(x)$ of surface waves, which we require in equation (4) as the input, we will follow the approach of Gal et al. (2018), where fast marching (Rawlinson & Sambridge, 2005) in combination with a phase velocity map is used to generate traveltimes and accounts for the deviation of raypaths from the great circle paths. In the underlying phase velocity map we use the updated maps USANT15 of Ekström (2017) at 10 and 20 s for Rayleigh and Love waves. For body waves we use the ak135 global traveltime model (Kennett, 2005).

Preproccesing of seismic data consists of power thresholding and filtering. To explain the thresholding method, let us consider the vertical component only. For a given seismic array, we compute the total power P at each station and generate a threshold value as the median of P across all stations in the array. If P at a certain station is smaller or higher than the threshold value by a factor of 10, the station is removed from any successive calculation. We apply this approach to all three components (Z, N, and E) independently and allow only stations which have power levels within the threshold boundaries on all three components to enter the MPF procedure. Stations with power levels outside of the threshold boundaries are likely affected by transient signals or instrumental errors which could lead to a bias in the MFP results. In the following we will analyze example cases of primary microseisms at 20 s and secondary microseisms at 10 s. We use a band-pass butterworth filter of the fourth-order between 19–21 s for the 20-s signal and 9.5–10.5 s for the 10-s signal.

These periods are chosen as a compromise between the requirement of a narrowband signal for the MFP procedure and the desire to study signals on short timescales. Removing the long period part of the signal leads to a delocalization in time (similar to a removal of the envelope/taper function) which leads to an averaging of the signal's spectral information. The source grid for the MFP approach is shown in Figure 1a. For the surface wave analysis we use a combination of USArray and XR stations displayed in Figure 1b. Body waves are analyzed with the majority of the USArray stations deployed in early 2010 (Figure 1c).

While these period bands lie on the borders of the primary and secondary microseism wavefield, they are chosen on purpose for this study. The advantage of using these periods is that "strong" (with respect to the selected frequency range) ocean-induced microseisms are not always present, and if they are, it is mainly from a single storm that has a very directive radiation pattern. This drastically reduces interference from multiple sources or directions and allows to evaluate the nature of the underlying wavefield.

2.4. Earthquake

To validate the technique, we first evaluate an earthquake in the southern Pacific region with a magnitude >6 mb (3 October 2009) before analyzing the short timescale microseism wavefield. A mix of USArray and XR stations (Figure 1b) is used for the analysis. After thresholding, we are left with 78 stations within a circular domain with a diameter of ~400 km. The surface wave train of the earthquake signal is analyzed at 20 s and filtered between 19 and 21 s.

We display the total power, coherence, and beam power in Figure 2 (Rayleigh waves a–c and Love waves d–f) on the same sample of data to illustrate the short timescale MFP technique. After band-pass filtering, we are left with a range of frequencies that comprises the signal and notably also creates a beat signal which will become of more importance when discussing microseisms. The total power is shown in Figures 2a and 2d and for a fixed frequency is a two-dimensional function which depends on the spatial coordinates and the source time. With increasing distance from each station the traveltime increases and the total power is shown as the sum of all station power contributions for a respective spatial point. Note that the total power (coherence and beam power) is dependent on $T(x)$ which is dependent on the traveltimes t_n to the spatial point x, and hence, for the same source time t_s the total power displays the power arriving at the array t_n later. For times which correspond to recordings with increased power, the total power plot shows this as an approximate circle (dependent on the velocity model and array geometry) of increased energy around the array. If we were to increase the source time, the circle of increased power would converge toward the stations.

The maximal total power for Rayleigh waves points toward the back azimuth of the source, but for Love waves it is perpendicular to the back azimuth which suggests that the Rayleigh wave signal is much stronger than the Love wave signal. Given that the examined earthquake epicenter is in the southern Pacific and Love waves propagate on average faster than Rayleigh waves, the Love wave energy should arrive at the array prior to that from Rayleigh waves. In our example, the energy of Love waves is mapped on an approximate circle with a radius larger than that of Rayleigh waves, and when source time is increased, it arrives at the same time as the Rayleigh wave energy. This happens because the total power is not correlated to a synthetic propagation model but a simple addition of all station powers. The result of this is that Rayleigh and Love wave energy is mixed and cannot be separated with the total power approach.

For the same data sample, the coherence is shown in Figures 2b and 2e. In contrast to the total power, the coherence is phase delay sensitive and shows where the coherent energy maps spatially for a fixed source time and frequency. For Rayleigh waves (Figure 2b), we observe an extended train of coherent energy that coincides with the mapped total energy (Figure 2a). It further shows that the signal is coherent not only at the maximum of the total power but also for a period of time before and after. For Love waves (Figure 2e), the coherence does not coincide with the total power which is mainly composed of Rayleigh waves but is observed to arrive prior to the energy of Rayleigh waves.

With our approach, we find coherence values of 0.9 and 0.65 for Rayleigh and Love waves, respectively. As a comparison, with conventional fk beamforming and a single 30-min window, we find coherence values of 0.38 and 0.01 for Rayleigh and Love waves. To fully understand the large difference between these values, we model the coherence as

$$C = m\frac{e_s}{e_{\text{tot}}}, \tag{6}$$

where e_s denotes the energy of the signal of interest, e_{tot} is the total energy in the analyzed time window, and m is a coefficient between 0 and 1 which accounts for the mismatch between synthetic and observed wavefield. If only a single signal is present, and there is no model mismatch, the coherence will be equal to 1. Increasing the number of signals in the analyzed time window will automatically decrease the coherence, even though all signals can follow the plane wave propagation model. Essentially, without any model error, the coherence yields the power ratios of the analyzed wavefield.

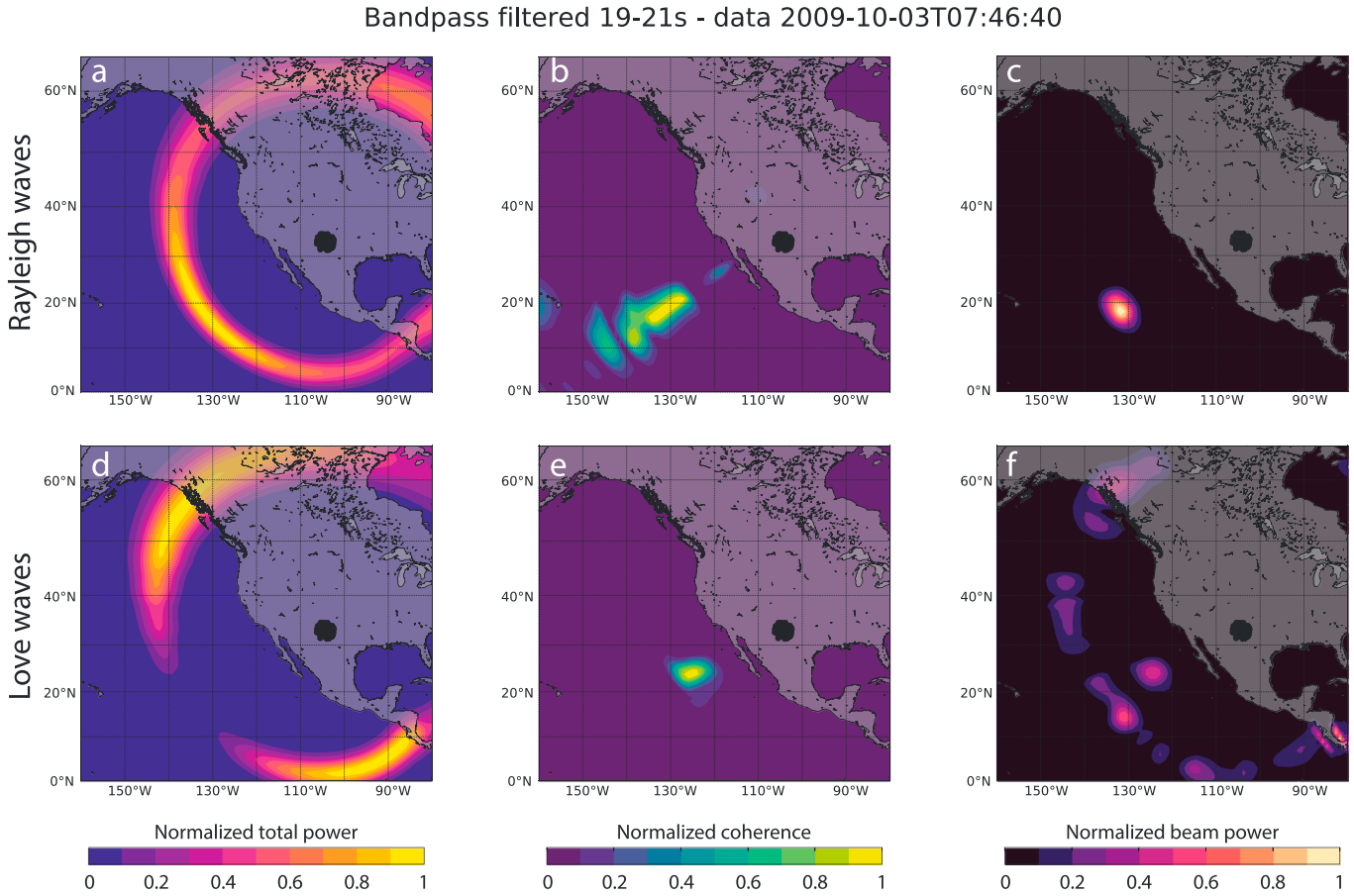

Figure 2. Analysis of an earthquake with the short timescale matched field processing approach. The top row shows normalized total power (a), normalized coherence (b), and normalized beam power of Rayleigh waves. The bottom row (d–f) displays the same quantities for Love waves. The above images are a snapshot at a particular source time which displays the earthquakes surface energy extending in time.

Given that our approach has a good time resolution, and only a small number of signals contribute due to the filtering and analytical signal approach, we are able to achieve high coherence, while the conventional approach will generally contain a mixture of signals. Additionally in the earthquake case, Rayleigh and Love waves arrive at different times, which allows us to evaluate them separately.

The beam power of our MFP approach, shown in Figures 2c and 2f, is a multiplication between the coherence and the total power, and hence, the result is an interplay between these two quantities. For Rayleigh waves (Figure 2c), the beam power highlights the incoming strongest wave train, while Love waves (Figure 2f) show an early arrival that coincides with the coherence (Figure 2e) and a second arrival that coincides with the total power (Figure 2d). The secondary arrival is the leaked Rayleigh wave energy. We have analyzed the leaked energy and found that only 1% of the radial energy leaked into the transverse component, but due to the lack of Love waves, the 1% is comparable in power to the Love waves.

It is important to stress that if we choose a slightly different frequency range for our bandpass filter, the result is likely to change, given that different frequencies contribute to the analyzed signal and additionally surface waves are dispersive which has an effect on the observed signal. Hence, it is important to state the bandwidth of the signal for reproducibility purposes.

3. Results

3.1. Primary and Secondary Microseism Surface Waves

We analyze primary microseisms at 20 s and secondary microseisms at 10 s. The period range has been chosen toward the higher end of each respective microseism band to avoid interference from too many active (spatially separated) microseism sources. In a trial run, we estimate the average coherence of secondary

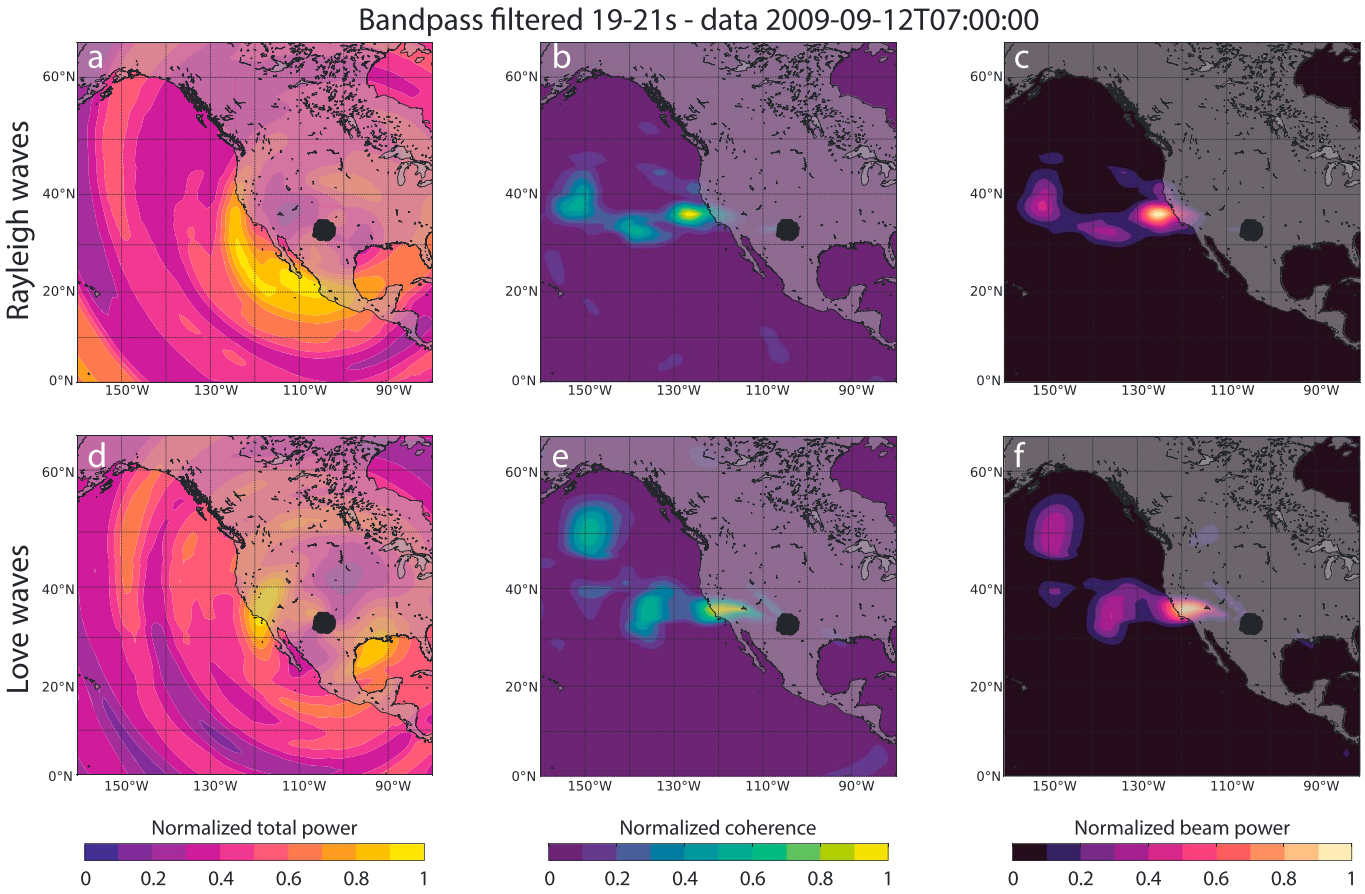

Figure 3. Analysis of primary microseisms with the short timescale matched field processing approach. The top row shows normalized total power (a), normalized coherence (b), and normalized beam power of Rayleigh waves. The bottom row (d–f) displays the same quantities for Love waves. The above images are a snapshot at a particular source time 2009-09-21T07:00:00.

microseisms with our approach for each day for the full year 2009. We find that coherence is higher when the microseism directionality is strongest. This is either the case for distant swells arriving at the West Coast of the United States and reflections being the dominant source of secondary microseisms (example spectrum for such a process is shown in Figure S1 in the supporting information) or large storm events in the North Atlantic which arrive at the array from a narrow back azimuth range.

We select a day (12 September 2009) for which the coherence reaches a maximal value, meaning that the signal is strongly directional and there are less interfering sources present compared to other days in 2009. The total power, coherence, and beam power are displayed in Figures 3 and 4 for primary and secondary microseisms, respectively. For completeness, the 12-hr time-averaged MFP results are shown in Figures S2 and S3.

We find that both primary and secondary microseisms display a pulse-like nature when observed on short timescales, contrary to the expected continuous nature (which would plot as a continuous beam of energy from the array toward the source in Figures 2 and 3). The observed beam powers in panels c and f of Figures 2 and 3 correspond well with the total energy (wave packages) that are estimated by the whole array. The pulses for primary microseisms appear more extended in time than secondary microseisms, which can be explained by twice as long the period of the underlying signal and the filtering used. If we allow longer periods to be present during the MFP procedure, the temporal extent of the pulses shortens.

In contrast to the earthquake case, we do not find a coherent stream of energy but a very similar picture between coherence and beam power. It is unclear whether this is the result of a real pulse nature of the microseisms wavefield or a combination of multiple continuous sources that combine to produce a beat signal.

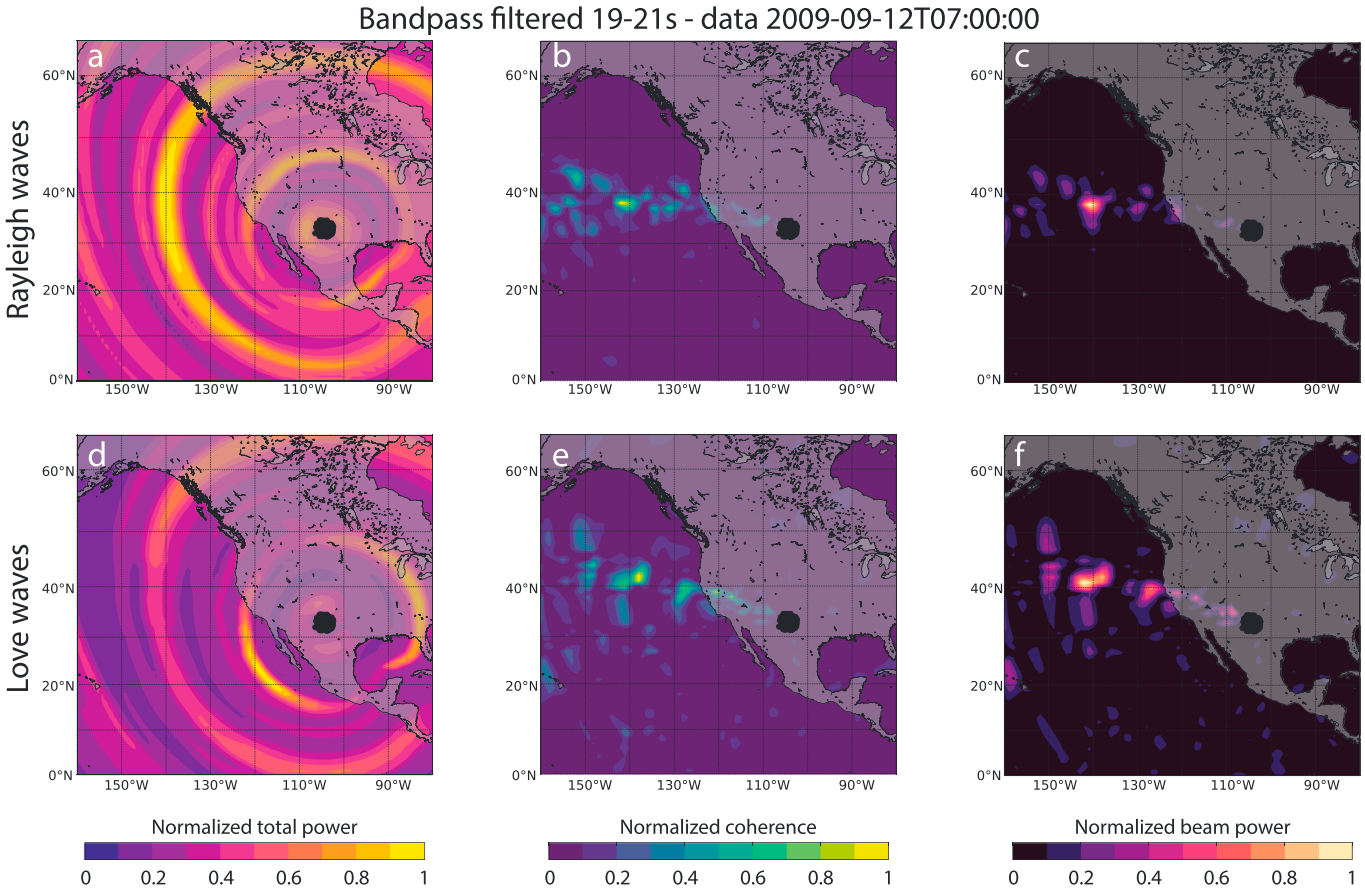

Figure 4. Analysis for secondary microseisms as outlined in the caption of Figure 3.

Averaging the beam power maps over the whole day with a 1-s source time interval leads to the same result as MFP with long time windows and temporal averaging over the cross-spectral density matrix (Figures S2 and S3). The advantage of our approach is that we can drastically increase the coherence given that fewer signals contribute during the MFP procedure on short timescales. When the full day is evaluated, we find pulses with an average coherence of ~0.4 and a maximal coherence of 0.91, while in the conventional time-averaged case the coherence value for the whole day is ~0.04 (these values have been obtained from the vertical component only for easier illustration). We will show in later stages how one can exploit the pulse nature and increased coherence to obtain novel information.

3.2. Pulse Properties

An indication for a continuous source in the ocean should be observable as a period pattern in the observed pulses. We have investigated the spectral nature of the total beam power and the beam power of our approach and did not find any spectral features which would confirm a period nature. Given that microseisms are generated by dynamic and time-dependent ocean swells, it is unclear on what timescales one could assume the microseism excitation source function over a respective area to be constant. It is much more likely that the microseism source function over an extended area is a superposition of many time-dependent point source functions which form the observed signal and hence no periodicities are observed.

To investigate if a correlation between Rayleigh and Love wave pulses exists, we perform a correlation analysis on their respective beam powers (for the same data—12 September 2009). For each spatial point (grid point), we perform our MFP analysis over the course of 12 hr with an interval of 1 s. The resulting power time series are then used to calculate the Pearson correlation coefficient between Rayleigh and Love waves for the same spatial coordinate. To avoid bias due to spurious features (we are interested whether the pulses correlate and not necessarily their respective strength), we divide the beam power into 30-min-long slices. The Pearson correlation is calculated for each of the 24 slices per spatial point, and the mean is used to

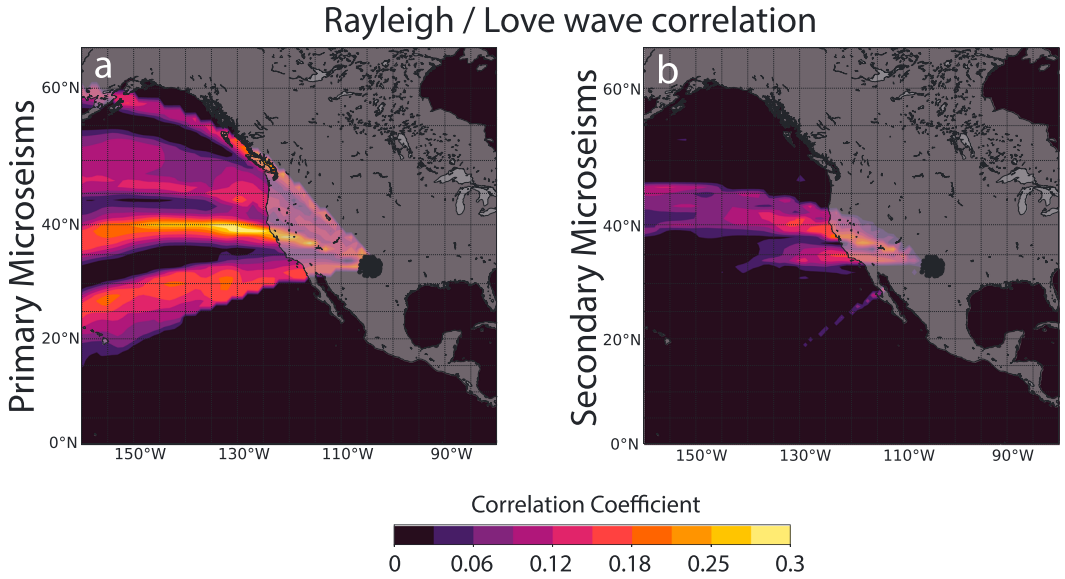

Figure 5. Pearson correlation coefficients between Rayleigh and Love wave beam powers for (a) primary and (b) secondary microseisms. The correlation coefficient is displayed only for back azimuths with a normalized beam power greater 0.2 (see Figures S2 and S3).

calculate the overall correlation coefficient. The resulting correlation maps are displayed in Figure 5. Additionally, we set the correlation coefficient to 0 when the combined normalized beam power (Figures S2 and S3) of Rayleigh and Love waves is lower then 0.2, because we are interested only in the dominant back azimuths. The maximal correlation values are 0.3 and 0.24 for primary and secondary microseisms, respectively, and indicate whether the two wave types are generated at the same time at a particular location.

The generation region of primary microseisms is linked to shallow bathymetry, and hence, the correlation between Rayleigh and Love wave pulses in deeper ocean (Figure 5a) does not arise from an actual excitation. The correlation follows certain back azimuths which suggests that pulses sometimes arrive earlier or later for each respective wave type. It is notable that the dominant back azimuth (Figure S2) yields a correlation close to 0, while other back azimuths show a mildly correlated signal. For secondary microseisms displayed in Figure 5b, the correlation is lower; maximal correlation is found on land and in this case the highest correlation coincides with the dominant back azimuth (Figure S3).

To test the uniqueness of the observed pulses, we have used a second array (700-km separation distance) and studied the wavefield for the same source time. The resulting observations displayed a different wavefield with very little correlation. To demonstrate why this is the case, we perform an internal correlation/coherence test on the first array to show how distance between stations and the station pair source geometry influences the coherence of the signal.

A 12-hr time series of the initial array is used to calculate the envelope functions from the analytical signals. The time series are realigned in time with calculated traveltimes from fast marching of group velocity maps (here we use group velocity because we will correlate the envelopes) to the estimated source location via time-averaged MFP. Similar to the case of pulse correlation, we divide the 12-hr record into 24 slices of 30 min and calculate the Pearson correlation between all station pairs as the mean of the 24 slices.

We select 3 days (8 February, 23 August, and 12 September) which have increased average pulse coherence and source-array distance (~1,200, ~4,500, and ~1,800 km). The approximate spatial generation regions of secondary microseisms for these days are marked in Figure 6a, and the traveltimes to these regions are used to realign the envelope time series for the correlation study. The correlation coefficient for all station pairs is summarized in a distance versus correlation coefficient versus average station-pair source angle β graph for each day in Figures 6b–6d. An illustration of β is shown in Figure 6a. For completeness, the scatter graphs from which the Figures 6b–6d were created can be found in the supporting information in Figure S4.

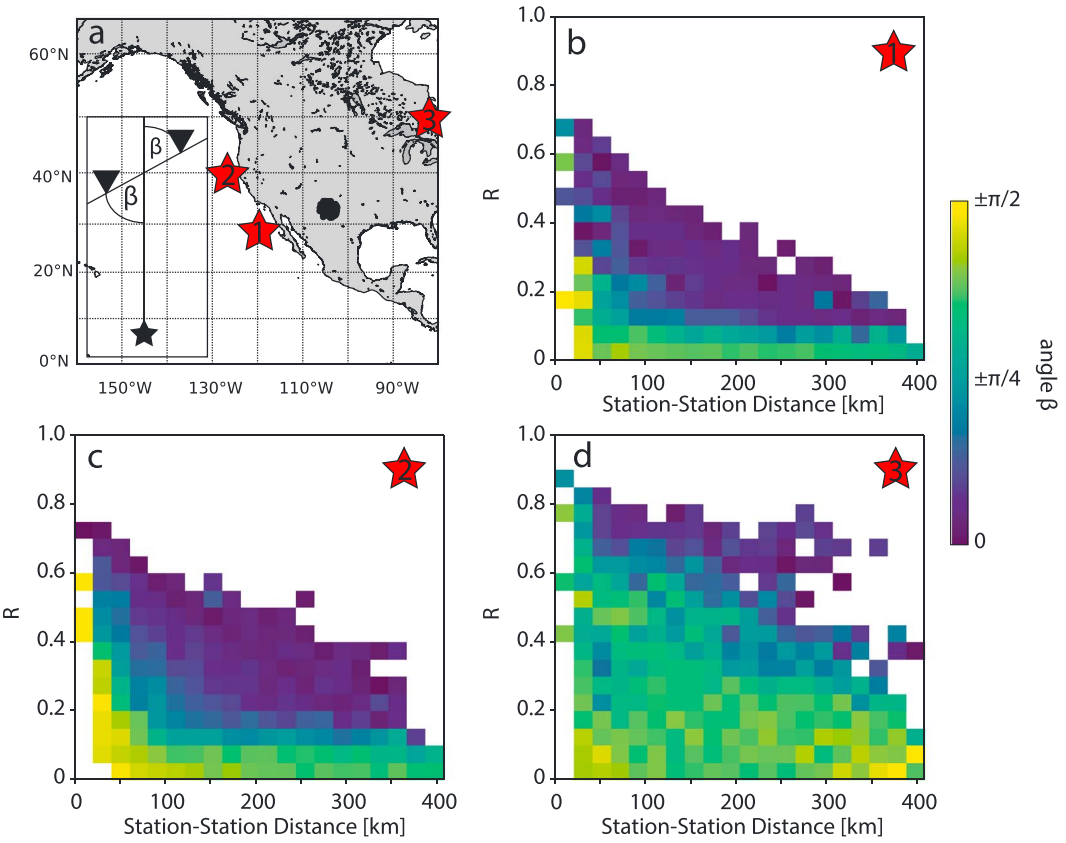

Figure 6. A graphic representation of the three example days are shown in (a), where the red stars denote the spatial source region of microseisms at each respective day. The array position is shown as a group of black dots. We embed a sketch of a single source (black star) and two receivers (black triangles) to visualize the angle β. Pearson correlation coefficient histograms are displayed for the three respective days (b) 8 February, (c) 12 September, and (d) 23 August.

Figure 6 shows a strong dependence on the station-station distance, array-source distance, and station-pair source angle. For the closest source (Figure 6b), we find a decline in correlation with increasing distance. This decline is strongly dependent on the angle β and shows that station pairs which are inline ($\beta = 0$) with the source have a higher correlation coefficient with increasing distance than station pairs with large β values which are found to be uncorrelated for station separations greater than 50 km. For the second source (Figure 6c), which is ~600 km further away we find the same pattern but a slower decline of the correlation coefficient with the distance. The third source (Figure 6d) is practically in the farfield, and the overall correlation coefficient is the highest, and we also find that stations with larger β values show correlations at larger distances.

To understand whether these features are unique to the wave packages, since we used the envelope to calculate the correlation, we perform a station-station-source coherence test which is sensitive to the phases. Instead of using the full array, we select a reference station and measure the coherence between the reference and all remaining stations. Similar to before, we use 12-hr-long time series and make use of our MFP approach, but for two stations at a time we only focused on a preselected source. The results are shown in Figure 7 for the same days, where sources (1, 2, and 3) from Figure 6a correspond to Figures 7a–7c). It should be noted that the coherence between two stations and a source yields values between 0 and 1. If two stations are uncorrelated, the coherence expectation value is 0.5 and everything smaller means anticorrelation while everything greater shows a correlation. The results in Figure 7 are in agreement with the previous approach. For the case where the sources are in the range of ~1,200–1,800 km (Figures 7a and 7b), we find that the wavefield is coherent at the dominant back azimuth and coherence decreases significantly on the direction perpendicular to the back azimuth. This coherence width seems to be source-station distance dependent as can be inferred from Figure 7a, where the coherence width is minimal and maximal in Figure 7c. If we select a different reference station, we observe similar behavior for all 3 days which strengthens these observations.

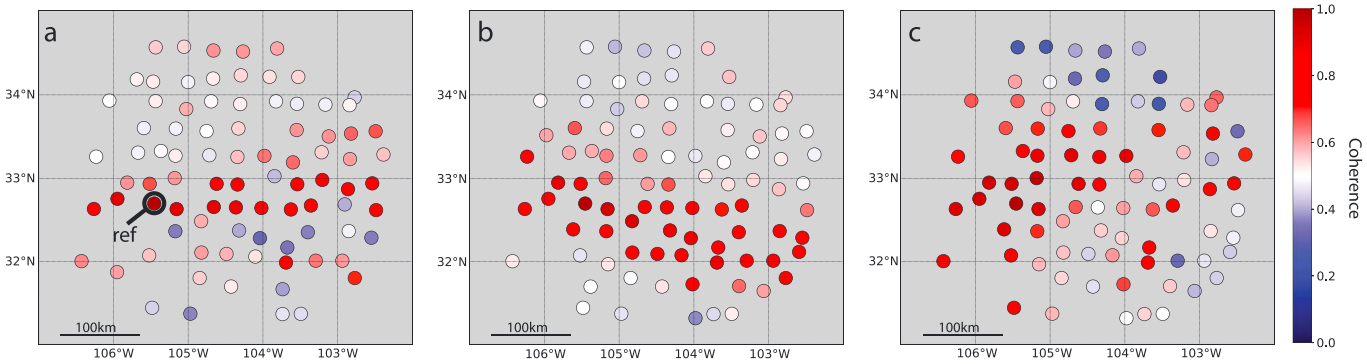

Figure 7. Station-station-source coherence values for the three respective days (a) 8 February, (b) 12 September, and (c) 23 August. Each circle represents one station, and the reference station is at 32.7°N to 105.4°W.

The above results are based on the average correlation/coherence during the 12-hr recording. If we examine these two quantities in more detail, we can find times at which most of the array is fully or minimally correlated/coherent. This shows that while the wavefield maintains a dominant back azimuth, the spatial correlation/coherence can vary strongly.

To shed light on the decrease of the correlation coefficient presented in Figure 6, we perform a simple synthetic example. For each of the 3 days, we select a source region (marked with the red stars in Figure 6a) and generate 100 synthetic sources within a radius of 100 km. The 100 synthetic sources represent our extended source in the ocean. The initial seismograms are generated in the frequency domain from a whitened signal,

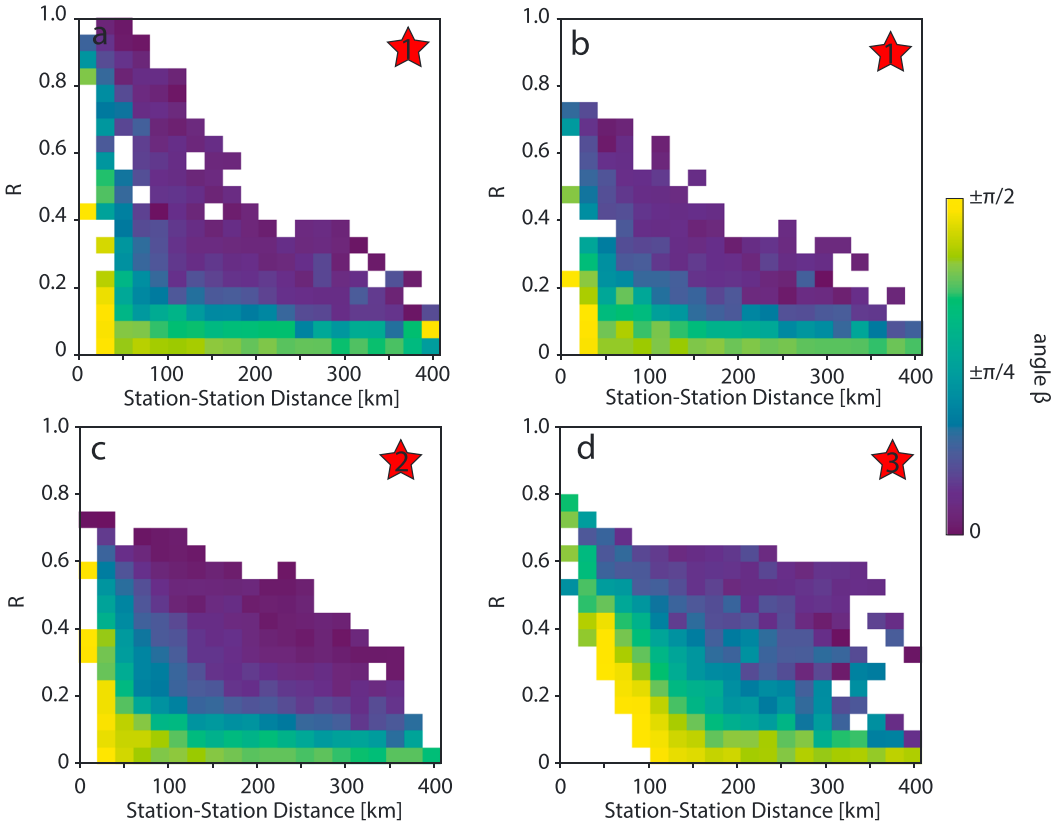

Figure 8. Pearson correlation coefficient histograms for synthetic data as in Figures 6b–6d. (a) Displays the Pearson correlation coefficient for the 8 February for an extended source but without any scattering/noise, while (b) is with noise. The 12 September and 23 August are shown in (c) and (d), respectively with noise.

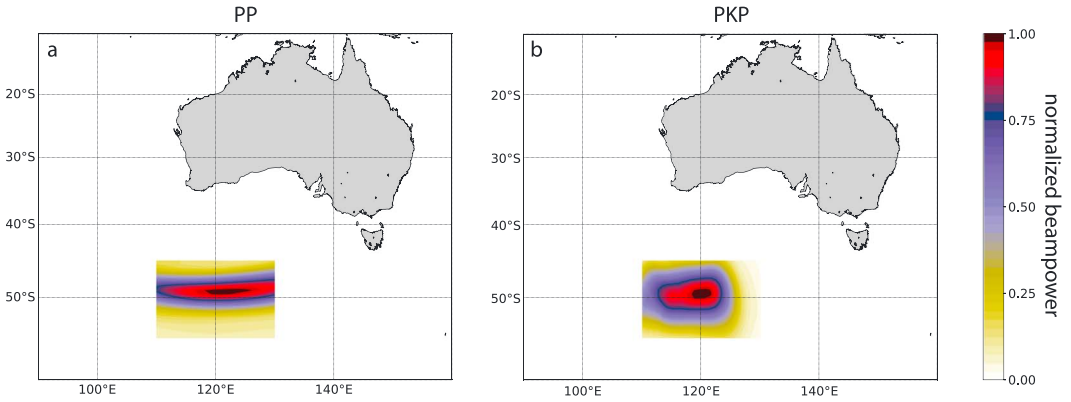

Figure 9. Conventional time-averaged matched field processing beam power results (filtered between 9.5- and 10.5-s period) for the (a) *PP* and (b) *PKP* phases. Only stations which are between 145 and 155° distance are permitted in this calculation.

that is, random phases and converted to the time domain. All 100 sources are combined (superpostion) to a single 12-hr time series per station and filtered and processed as the observed data.

When cross correlation of the synthetic pulses is performed the same way as in the observed data case, we find a similar dependence displayed in Figure 8a for the 8 February. In contrast to the observed data case, the correlation between "inline" stations with short distances is close to 1, while in the observed data case, the correlation is below 0.8. This can be addressed by either including some type of scattering or simply generating another 100 synthetic sources with random coordinates (these essentially act as noise). When we add another 100 randomly distributed point source, we find a good match between synthetic and observed results (Figure 8b). The results for the 12 September and 23 August can be found in Figures 8c and 8d.

For the two examples from the West Coast, we find a good match between observed and synthetic data. The slope of the correlation function is given by the extent of the synthetic source and the source-array distance. For the 23 August (Figure 8d), this simple model does not recreate the observed behavior, because the added noise (100 randomly originating sources) modifies the waveforms too much. If one would reduce the noise, the two results would be in better agreement. This could be a likely scenario since the source is further away than in the first two cases, and the wavefield could have been cleaned on the way toward the array.

With the above synthetic example, we show that the likely controls on correlation coefficient decrease are the source extent and the path propagation effects.

3.3. Body Waves

To analyze body waves on short timescales, we are confined to the frequency range of secondary microseisms where *P* waves can be the dominant part of the wavefield. The MFP procedure stays largely the same but requires traveltimes which are calculated from a *P* wave reference model for which we utilize ak135 (first arrivals for *PP* and *PKP* are used here). An ideal opportunity to study *P* waves occurred on 1 February 2010, where a storm in the Southern Indian Ocean produced strong and approximately spatially stationary microseisms in the form of *PKP* waves (Retailleau et al., 2018). Additionally, the generated secondary microseisms are in the range of 9–11 s and hence in a period range with very few other interfering signals (other microseisms sources) making it ideal for our study. In the following, we make use of all available USArray stations which were operational at this time and also all other stations (all freely available data from IRIS) with an LHZ channel that are within the deployment area of the USArray. Preprocessing follows the above outlined filtering and thresholding techniques, and we are left with 328 stations for the wavefield analysis.

Conventional time-averaged MFP results (12 hr, 1 February 2010) are displayed in Figure 9a for *PP* and Figure 9b for *PKP* waves. In both cases, the signal is spatially well confined and optimal for a short timescale analysis. When evaluated with our MFP technique, we find the properties of *PKP* waves to be similar to the surface wave case. Instead of a continuous signal, we find pulses to arrive from the distance source. The pulses correlate with the total power of the signal and the coherence.

We analyze the *PKP* signal with the station-station-source correlation/coherence approach as in the surface waves case. The source-station distance is displayed in Figure 10a, and the envelope Pearson correlation and

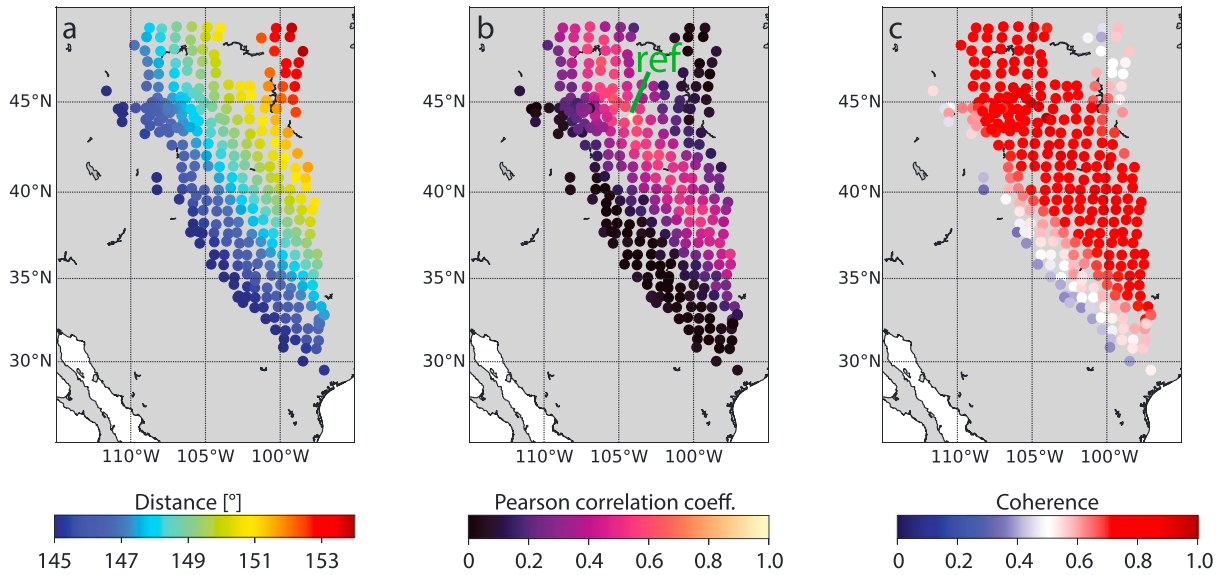

Figure 10. (a) Source-station distance of the *PKP* phase. Only stations which are between 145° and 155° distance are permitted in this calculation. (b) Pearson correlation coefficient calculated from the envelopes of the signal between one reference station and all other stations. The reference station is located at 44.1°N to 104.0°W and visible as a yellow circle in (b). (c) Station-station-source coherence calculated from the phases of the wavefield.

phase coherence can be found in Figures 10b and 10c, respectively. For both the correlation and coherence, we find a pattern that is strongly dependent on the epicentral distance, while the azimuthal direction shows a much smaller dependence. The epicentral dependence is found to be more pronounced for the case of total power correlation in Figure 10b compared to the coherence in Figure 10c. This pattern is the opposite of surface waves, and potential reasons for this finding are explored in the discussion.

3.4. Utilizing the Pulse Nature

The observation of pulses in the microseism wavefield with a coherence measure, that is, the measure of a match between observed and synthetic models, can be used for array self calibration purposes. We will demonstrate this for the body wave case first, where the source location can be constrained and will discuss an approach for surface waves as well. We make use of the 1 February 2010 *PKP* source in the Southern Indian Ocean. The analysis in this section is carried out on vertical component data only but can readily be extended to three components.

The first step is to select the spatial source location (Figure 9) to focus the array on and evaluate 12 hr of secondary microseism *PKP* waves with our MFP approach. The analysis results in a coherence time series that tells us at which source times the coherence is large, that is, a good match between the observed and synthetic wavefields. An example of the 1-D coherence function can be found in Figure 11a. The coherence time series is used to find all local maxima, and only the source times corresponding to coherence that exceeds 50% of the largest coherence measured are retained.

In the second step, we calculate the phase deviation $\phi_n(f, T(x))$ from the relative mean phase of $\tilde{X}_n(f, T(x))$ as

$$\phi_n(f, T(x)) = \tilde{X}_n(f, T(x)) \left[\frac{1}{K} \sum_n \tilde{X}_n(f, T(x)) \right]^*, \tag{7}$$

where $*$ denotes the complex conjugate. The average phase deviation is then calculated as the mean from all accepted local source time maxima. Since we know that our signal is centered around a period of 10 s, the phase delay can be translated into a relative time delay which is shown in Figure 11b for each station of the array. If these delays are added to the traveltime inferred from ak135, we obtain calibrated traveltimes which result in a improved coherence function which is shown in Figure 11a. If the calibration is run again with the improved traveltimes, we find a much improved relative time delay result shown in Figure 11c. These time delays are only relative in nature in the sense that we do not really estimate the actual traveltime but the delays at which phases are measured between stations. Nevertheless, this approach is capable of

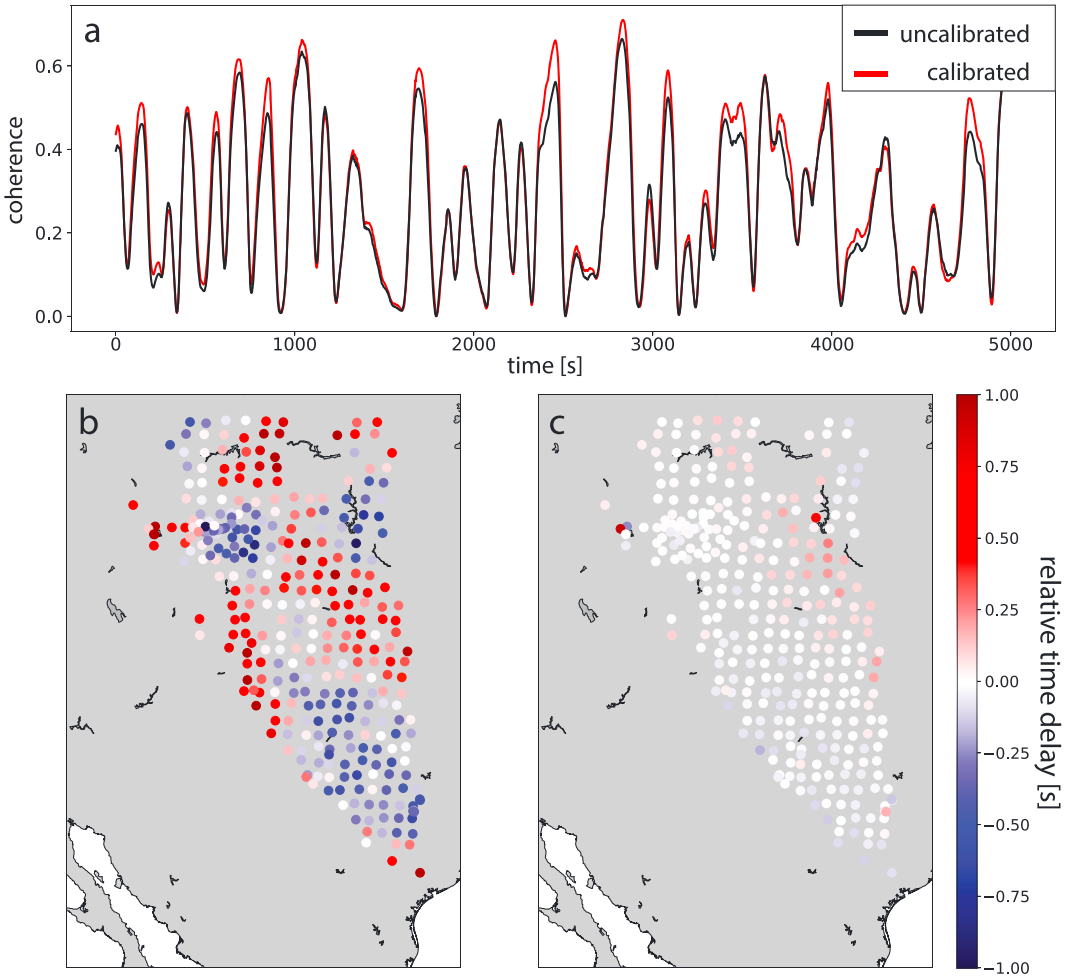

Figure 11. (a) Example of the coherence function estimated with the USArray on the *PKP* source in the Southern Indian Ocean for the ak135 model (black line) and calibrated time delays owing to the pulse nature (red line). Twelve hours have been used to obtain calibrated relative time delays, but only 5,000 s are displayed for visualization purposes. (b) Illustration of the relative time delay per station estimated by via the calibration method and (c) the relative time delay when we account for the calibrated relative time delays.

revealing some structural information by using a 12-hr recording, given an optimal source exists. The calibrated coherence function is ~10% larger on average. It should be noted that calibrating the array with *PKP* waves from a particular source does not calibrate the array for the *PP* wavefield from the same source given the differing slownesses and sampling of the Earth.

The above result was easily obtained due to the dominant and stationary nature of the microseism source (which is quite rare). In general, microseism body wave sources are generated over a wide area and move with time. With the simple approach of focusing the array on one spatial location, one would bias the calibration if energy is generated from a wider area. A possible solution is to estimated pulses from a wider source grid and assign a pulse to a spatial coordinate where its coherence is maximal and estimate the time delay for each spatial coordinate. We have experimented with this approach and suspect that a large statistical sample (multiple storms generating dominant microseism *P* waves at the same spatial location) is required to obtain robust results.

For surface waves, we chose a general approach to show the applicability of the calibration technique. We start off with conventional fk beamforming to estimate the phase velocity of Rayleigh waves at 10 s ($v_p = 3.14$ km/s), which we use as the reference velocity to generate interstation phase delays. With a fixed phase velocity and frequency, the fk beamformer is a one-dimensional function dependent on the back azimuth. Our objective is to calibrate the phase delays $\phi_n(\theta)$ for discretized back azimuths θ. To observe

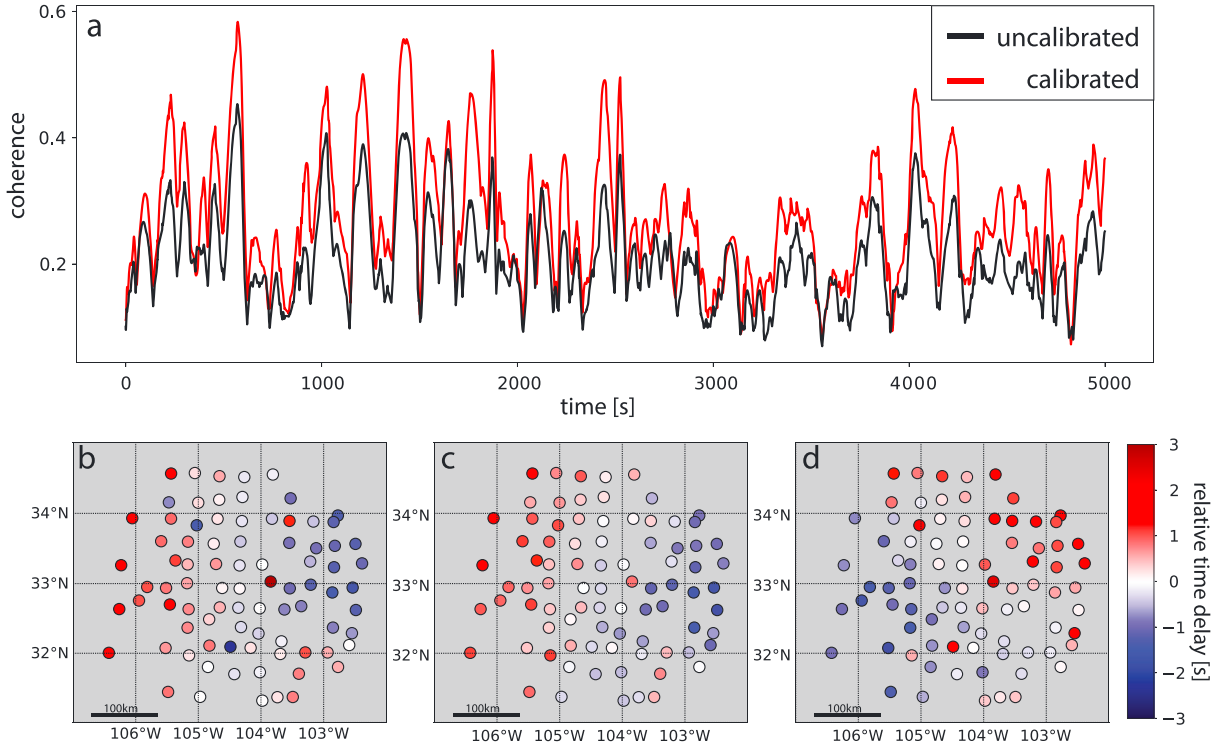

Figure 12. (a) Coherence functions as in Figure 10a but for surface waves. (b–d) Relative time delays displayed for the three example days, (b) 8 February, (c) 12 September, and (d) 23 August.

pulses with beamforming, we implement filtering, the analytical signal, and trace alignment which will make the beamformer dependent on source time as well.

We have applied this type of beamformer for the first 200 days in the year 2009. For each day we calculate the coherence $P_C(\theta, T(x))$ and the relative phase delays of each pulse are assigned to a back azimuth $\phi_n(\theta)$ which is discretized into 5° bins. In this case, only the source times of the top 10% largest coherent events are retained.

The coherence function $P_C(\theta, T(x))$ for the 12 September 2009 is shown in Figure 12a with and without calibration applied. The day is selected as it lies outside of the 200 days, and no bias due to the calibration procedure is expected. We find an average coherence increase of 35% with the calibrated data sets which directly translates into a 35% higher beam power. For visualization purposes, we display the relative time delay for the previously analyzed 3 days (8 February, 23 August, and 12 September) in Figures 12b–12d, by displaying the relative traveltimes for the dominant back azimuth for that respective day. All 3 days display a source-station distant-dependent pattern which suggests that the phase velocity propagates faster than previously estimated with fk beamforming. The phase velocity estimated via the pulse calibration method is on average 2–3% faster than the one from fk beamforming. When compared to the preestimated phase velocities (USANT15) used for our MFP approach, we find comparable coherence functions.

This approach demonstrates that it is not required to have access to phase velocity maps in order to calibrate a seismic array, and this should be especially useful for arrays that suffer from strong velocity heterogeneities.

4. Discussion

In the following section we discuss the optimal frequency bandwidth for future studies, whether microseisms are continuous or pulsed and the reason for the correlation patterns observed for surface and *PKP* waves.

In this study, we chose the band-pass width in a heuristic manner as a trade-off between time resolution and the narrowband requirement of MFP to showcase that coherent energy arrives at the receiver in form of pulses. In future studies this band-pass width can be tuned for a specific purpose, for instance, the

maximization of the coherence function. This will likely be wavefield and seismic array specific and can be estimate in a "calibration" routine.

The observation of pulses seems counterintuitive to the commonly accepted continuous nature of the ambient noise wavefield; however, these two views are not mutually exclusive. Given the large spatial extent over which microseisms are generated, a multitude of ocean waves contributes to the generation of seismic waves. It is therefore safe to assume that in a large enough area microseisms are continuously excited. The coherence measure presented in this work is not able to distinguish whether the pulses are purely the result of superposition of waveforms or a signal beat. It is likely the observed wavefield is a combination of both. We have tested if the pulse shape is caused by incoherent stations participating but found the pulse shape to be present even with smaller arrays.

Our correlation/coherence results from section 3.2 support the view that multiple source functions contribute to the observed waveform. For a spatially extended source, we find that correlation/coherence decreases faster with distance if the array is closer to the source (Figures 6b and 8b). This indicates that the wavefield is highly variable given that the signal has components over a broader back azimuth. This is further illustrated for large values of β, where the wavefield displays uncorrelated behavior. For a spatially extended source in the far field (Figures 6d and 8d), the correlation/coherence is much greater even for larger values of β suggesting that the wavefield is much more similar over a larger area. Dispersion of surface waves does not seem to play a major role, given that the observed frequency range is quite narrow compared to the aperture and velocity of surface waves. Path propagation effects and specifically focusing can have a large contribution since multiple back azimuths are merged into a smaller range.

For *PKP* waves we observe a correlation/coherence pattern which decreases strongly with distance but less in azimuthal direction, that is, the opposite of surface waves. The ocean site effect amplification factor (Gualtieri et al., 2013) displays a difference of 5% between the take-off angles of 6.28° and 10.17° (145–155° distance) and hence is not responsible for the loss in correlation/coherence. One possibility is that the transition between the core mantle boundary has a strong effect on the phase which results in a decorrelation of the wavefield with respect to the source-station distance. Another possibility lies in the multipathing nature of the *PKP* phase, which has two arrivals between 145° and 155° distance. The time difference between the two arrivals varies strongly on distance, which results in a different superposition of the wavefield with varying source-station distance.

5. Conclusion

We have analyzed the primary and secondary microseism wavefields on short timescales and found that coherent energy reaches the array in form of pulses rather than a continuous signal. The pulses are strongly frequency dependent and show unique correlation patterns dependent on the wave types. Surface wave pulses correlate well when the source and two receiving stations are in line and do not correlate if the line between two station is perpendicular to the back azimuth of the source. *PKP* waves show the opposite effect, where the correlation decreases with increasing source-station distance, while correlation is mildly decreasing for azimuthally distributed stations at the same source-station distance. These effects can be attributed to source and path propagation effects.

The observed pulse nature has been utilized to self-calibrate a seismic array and improve relative traveltimes between stations. For the particular array used, we find an average improvement of 10% for *PKP* waves in comparison to ak135 and an average improvement of 35% for surface waves compared to a plane wave model. Larger benefits can be expected for arrays that suffer from strong velocity heterogeneities.

Acknowledgments
We thank two anonymous reviewers for their comments which have improved this work. We acknowledge data access through the IRIS DMC (https://ds.iris.edu/ds/nodes/dmc/). We thank the Tasmanian Partnership for Advanced Computing (TPAC), which enabled the access to its HPC Facilities. This study is funded by the Australian Research Council under project DP150101005. We thank Michael Ritzwoller and members of the CIEI at Colorado University Boulder where AMR was hosted as a Fulbright Senior Scholar in 2017.

References

Ardhuin, F. (2018). Large-scale forces under surface gravity waves at a wavy bottom: A mechanism for the generation of primary microseisms. *Geophysical Research Letters*, *45*, 8173–8181. https://doi.org/10.1029/2018GL078855

Ardhuin, F., Gualtieri, L., & Stutzmann, E. (2015). How ocean waves rock the Earth: Two mechanisms explain microseisms with periods 3 to 300 s. *Geophysical Research Letters*, *42*, 765–772. https://doi.org/10.1002/2014GL062782.1

Baggeroer, A., Kuperman, W., & Mikhalevsky, P. (1993). An overview of matched field methods in ocean acoustics. *IEEE Journal of Oceanic Engineering*, *18*(4), 401–424. https://doi.org/10.1109/48.262292

Berger, J., Davis, P., & Ekström, G. (2004). Ambient Earth noise: A survey of the global seismographic network. *Journal of Geophysical Research*, *109*, B11307. https://doi.org/10.1029/2004JB003408

Bromirski, P., & Duennebier, F. (2002). The near-coastal microseism spectrum: Spatial and temporal wave climate relationships. *Journal of Geophysical Research*, *107*(B8), 5–20. https://doi.org/10.1029/2001JB000265

Campillo, M., & Paul, A. (2003). Long-range correlations in the diffuse seismic coda. *Science*, *299*(5606), 547–9. Retrieved from http://www.ncbi.nlm.nih.gov/pubmed/12543969. https://doi.org/10.1126/science.1078551

Corciulo, M., Roux, P., Campillo, M., Dubucq, D., & Kuperman, W. A. (2012). Multiscale matched-field processing for noise-source localization in exploration geophysics. *Geophysics*, *77*(5), KS33–KS41. https://doi.org/10.1190/geo2011-0438.1

Ekström, G. (2017). Short-period surface-wave phase velocities across the conterminous United States. *Physics of the Earth and Planetary Interiors*, *270*, 168–175. Retrieved from http://www.sciencedirect.com/science/article/pii/S0031920117301942. https://doi.org/10.1016/j.pepi.2017.07.010

Euler, G. G., Wiens, D., & Nyblade, A. A. (2014). Evidence for bathymetric control on the distribution of body wave microseism sources from temporary seismic arrays in Africa. *Geophysical Journal International*, *197*(3), 1869–1883. https://doi.org/10.1093/gji/ggu105

Farra, V., Stutzmann, E., Gualtieri, L., Schimmel, M., & Ardhuin, F. (2016). Ray-theoretical modeling of secondary microseism *P* waves. *Geophysical Journal International*, *206*(3), 1730–1739. https://doi.org/10.1093/gji/ggw242

Friedrich, A., Klinge, K., & Krüger, F. (1998). Ocean-generated microseismic noise located with the Graefenberg array. *Journal of Seismology*, *2*(1), 47–64. Retrieved from http://ezproxy.utas.edu.au/login?url=http://search.proquest.com/docview/887420566?accountid=14245

Gal, M., & Reading, A. M. (2018). *Chapter 2: Beamforming and polarisation analysis*. Cambridge, UK: Seismic Ambient Noise, Cambridge University Press.

Gal, M., Reading, A. M., Ellingsen, S. P., Gualtieri, L., Koper, K. D., Burlacu, R., & Tkalčić, H. (2015). The frequency dependence and locations of short-period microseisms generated in the Southern Ocean and West Pacific. *Journal of Geophysical Research: Solid Earth*, *120*, 5764–5781. https://doi.org/10.1002/2015JB012210

Gal, M., Reading, A. M., Rawlinson, N., & Schulte-Pelkum, V. (2018). Matched field processing of three-component seismic array data applied to Rayleigh and Love microseisms. *Journal of Geophysical Research: Solid Earth*, *123*, 6871–6889. https://doi.org/10.1029/2018JB015526

Gerstoft, P., Shearer, P. M., Harmon, N., & Zhang, J. (2008). Global *P*, *PP*, and *PKP* wave microseisms observed from distant storms. *Geophysical Research Letters*, *35*, 23306. https://doi.org/0.1029/2008GL036111

Gualtieri, L., Stutzmann, E., Capdeville, Y., Ardhuin, F., Schimmel, M., Mangeney, A., & Morelli, A. (2013). Modelling secondary microseismic noise by normal mode summation. *Geophysical Journal International*, *193*(3), 1732–1745. Retrieved from http://gji.oxfordjournals.org/cgi/doi/10.1093/gji/ggt090. https://doi.org/10.1093/gji/ggt090

Gutenberg, B. (1936). On microseisms. *Bulletin of the Seismological Society of America*, *26*(2), 111–117. Retrieved from http://bssa.geoscienceworld.org/content/26/2/111.refs

Hasselmann, K. (1963). A statistical analysis of the generation of microseisms. *Reviews of Geophysics*, *1*(2), 177–210. https://doi.org/10.1029/RG001i002p00177

Haubrich, R., Munk, W., & Snodgrass, F. (1963). Comparative spectra of microseisms and swell. *Bulletin of the Seismological Society of America*, *53*(1), 27–37.

Kennett, B. (2005). *Seismological tables: ak135*. Australia: Research School of Earth Sciences, The Australian National University. Retrieved from http://www.researchgate.net/publication/257584026_AK135tables/file/72e7e52573ae24bc7a.pdf

Koper, K. D., & Burlacu, R. (2015). The fine structure of double-frequency microseisms recorded by seismometers in North America. *Journal of Geophysical Research: Solid Earth*, *120*, 1677–1691. https://doi.org/10.1002/2014JB011820

Koper, K. D., de Foy, B., & Benz, H. (2009). Composition and variation of noise recorded at the Yellowknife Seismic Array, 1991-2007. *Journal of Geophysical Research*, *114*, B10310. https://doi.org/10.1029/2009JB006307

Koper, K. D., Seats, K., & Benz, H. (2010). On the composition of Earth's short-period seismic noise field. *Bulletin of the Seismological Society of America*, *100*(2), 606–617. https://doi.org/10.1785/0120090120

Lacoss, R., Kelly, E., & Toksöz, M. (1969). Estimation of seismic noise structure using arrays. *Geophysics*, *34*(1), 21–38. https://doi.org/10.1190/1.1439995

Landès, M., Hubans, F., Shapiro, N. M., Paul, A., & Campillo, M. (2010). Origin of deep ocean microseisms by using teleseismic body waves. *Journal of Geophysical Research*, *115*, B05302. https://doi.org/10.1029/2009JB006918

Legaz, A., Revil, A., Roux, P., Vandemeulebrouck, J., Gouédard, P., Hurst, T., & Bolève, A. (2009). Self-potential and passive seismic monitoring of hydrothermal activity: A case study at Iodine Pool, Waimangu geothermal valley, New Zealand. *Journal of Volcanology and Geothermal Research*, *179*(1), 11–18. Retrieved from http://www.sciencedirect.com/science/article/pii/S0377027308005349. https://doi.org/10.1016/j.jvolgeores.2008.09.015

Liu, Q., Koper, K. D., Burlacu, R., Ni, S., Wang, F., Zou, C., & Reading, A. M. (2016). Source locations of teleseismic P, SV, and SH waves observed in microseisms recorded by a large aperture seismic array in China. *Earth and Planetary Science Letters*, *449*, 39–47. https://doi.org/10.1016/j.epsl.2016.05.035

Longuet-Higgins, M. (1950). A theory of the origin of microseisms. *Philosophical Transactions of the Royal Society of London. Series A. Mathematical and Physical Sciences*, *243*, 857. Retrieved from http://www.jstor.org/stable/10.2307/91470

McNamara, D. E., & Buland, R. P. (2004). Ambient noise levels in the continental United States. *Bulletin of the Seismological Society of America*, *94*(4), 1517. https://doi.org/10.1785/012003001

Rawlinson, N., & Sambridge, M. (2005). The fast marching method: An effective tool for tomographic imaging and tracking multiple phases in complex layered media. *Exploration Geophysics*, *36*(4), 341–350. https://doi.org/10.1071/EG05341

Reading, A. M., Koper, K. D., Gal, M., Graham, L. S., Tkalčić, H., & Hemer, M. A. (2014). Dominant seismic noise sources in the Southern Ocean and West Pacific, 2000–2012, recorded at the Warramunga Seismic Array, Australia. *Geophysical Research Letters*, *10*, 3455–3463. https://doi.org/10.1002/2014GL060073

Retailleau, L., Lands, M., Gualtieri, L., Shapiro, N. M., Campillo, M., Roux, P., & Guilbert, J. (2018). Detection and analysis of a transient energy burst with beamforming of multiple teleseismic phases. *Geophysical Journal International*, *212*(1), 14–24. https://doi.org/10.1093/gji/ggx410

Rost, S., & Thomas, C. (2002). Array seismology: Methods and applications. *Reviews of Geophysics*, *40*(3), 1008. https://doi.org/10.1029/2000RG000100

Rost, S., & Thomas, C. (2009). Improving seismic resolution through array processing techniques. *Surveys in Geophysics*, *30*(4-5), 271–299. https://doi.org/10.1007/s10712-009-9070-6

Roux, P., Sabra, K. G., Kuperman, W. A., & Roux, A. (2005). Ambient noise cross correlation in free space: Theoretical approach. *The Journal of the Acoustical Society of America*, *117*(1), 79–84. https://doi.org/10.1121/1.1830673

Saito, T. (2010). Love-wave excitation due to the interaction between a propagating ocean wave and the sea-bottom topography. *Geophysical Journal International*, *182*(3), 1515–1523. https://doi.org/10.1111/j.1365-246X.2010.04695.x

Schimmel, M., Stutzmann, E., Ardhuin, F., & Gallart, J. (2011). Polarized Earth's ambient microseismic noise. *Geochemistry, Geophysics, Geosystems*, *12*, Q07014. http://doi.wiley.com/10.1029/2011GC003661

Schulte-Pelkum, V., Earle, P. S., & Vernon, F. L. (2004). Strong directivity of ocean-generated seismic noise. *Geochemistry, Geophysics, Geosystems*, *5*, Q03004. https://doi.org/10.1029/2003GC000520

Shapiro, N. M., & Campillo, M. (2004). Emergence of broadband Rayleigh waves from correlations of the ambient seismic noise. *Geophysical Research Letters*, *31*, L07614. https://doi.org/10.1029/2004GL019491

Snieder, R., & Hagerty, M. (2004). Monitoring change in volcanic interiors using coda wave interferometry: Application to Arenal Volcano, Costa Rica. *Geophysical Research Letters*, *31*, L09608. https://doi.org/10.1029/2004GL019670

Stutzmann, E., Ardhuin, F., Schimmel, M., Mangeney, A., & Patau, G. (2012). Modelling long-term seismic noise in various environments. *Geophysical Journal International*, *191*(2), 707–722. https://doi.org/10.1111/j.1365-246X.2012.05638.x

Stutzmann, E., Roult, G., & Astiz, L. (2000). GEOSCOPE station noise levels. *Bulletin of the Seismological Society of America*, *90*(3), 690–701. https://doi.org/10.1785/0119990025

Stutzmann, E., Schimmel, M., Patau, G., & Maggi, A. (2009). Global climate imprint on seismic noise. *Geochemistry, Geophysics, Geosystems*, *10*, Q11004. https://doi.org/10.1029/2009GC002619

Toksöz, M., & Lacoss, R. (1968). Microseisms: Mode structure and sources. *Science*, *159*, 872–873. Retrieved from http://www.sciencemag.org/content/159/3817/872.short

Tromp, J., Luo, Y., Hanasoge, S., & Peter, D. (2010). Noise cross-correlation sensitivity kernels. *Geophysical Journal International*, *183*(2), 791–819. https://doi.org/10.1111/j.1365-246X.2010.04721.x

Vandemeulebrouck, J., Roux, P., Gouedard, P., Legaz, A., Revil, A., Hurst, A., & Jardani, A. (2010). Application of acoustic noise and self-potential localization techniques to a buried hydrothermal vent (Waimangu Old Geyser site, New Zealand). *Geophysical Journal International*, *180*(2), 883–890. https://doi.org/10.1111/j.1365-246X.2009.04454.x

Wiechert, E. (1904). Verhandlungen der zweiten internationalen Seismologischen Konferenz. Gerlands Beitraege zur Geophysik, Ergaenzungsband. II: 41-43 (in German).